Desalination and Water Treatment
www.deswater.com
doi: 10.5004/dwt.2020.26067

196 (2020) 329–347
August

Honeycomb-like porous-activated carbon derived from gasification waste for malachite green adsorption: equilibrium, kinetic, thermodynamic and fixed-bed column analysis

Anis Atikah Ahmad[a,b,c,†], Mohd Azmier Ahmad[a,*], Nasehir Khan EM Yahaya[d], Azam Taufik Mohd Din[a], Ahmad Radi Wan Yaakub[b]

[a]*School of Chemical Engineering, Engineering Campus, Universiti Sains Malaysia, 14300 Nibong Tebal, Penang, Malaysia, Tel. +604-599 6459, Fax: +604-599 6908; email: chazmier@usm.my (M.A. Ahmad)*

[b]*School of Bioprocess Engineering, Universiti Malaysia Perlis, Kompleks Pusat Pengajian Jejawi 3, 02600 Arau, Perlis, Malaysia*

[c]*Centre of Excellence for Biomass Utilization, School of Bioprocess Engineering, Universiti Malaysia Perlis, Kompleks Pusat Pengajian Jejawi 3, Arau, 02600 Perlis, Malaysia*

[d]*National Hydraulic Research Institute of Malaysia (NAHRIM), Ministry of Environment and Water, Lot 5377, Jalan Putra Permai, 43300 Seri Kembangan, Selangor, Malaysia*

Received 9 December 2019; Accepted 2 May 2020

ABSTRACT

In this study, the preparation conditions for the gasification waste-based activated carbon (GWAC) were optimized with malachite green (MG) dye removal and GWAC yield as responses. The adsorption equilibrium, kinetic behavior, and thermodynamics properties were also analyzed. The optimum conditions for synthesizing GWAC were found at a radiation power, time, and impregnation ratios of 616 W, 1 min, and 1.06 g g^{-1}, respectively, which resulted in an 89.98% yield of GWAC and 99.01% MG removal. This sample shows the surface area and total pore volume of 351.92 m^2 g^{-1} and 0.22 cm^3, respectively. For the isotherm study, the Fritz–Schlünder model fitted the adsorption data very well with an R^2 value of 0.9919–0.9932. The results of the kinetic study showed that the MG adsorption followed a pseudo-first-order kinetic model (R^2 = 0.9625–0.9871). The film diffusion was found to be the rate-limiting step of MG adsorption. The adsorption of the MG dye onto GWAC was an endothermic and spontaneous process with ΔH of 9.183 kJ mol^{-1}. In continuous mode, Thomas and Yoon–Nelson models successfully predicted the MG adsorption on the GWAC. GWAC demonstrates its commercial feasibility based on a low production cost of 0.23 USD kg^{-1}.

Keywords: Gasification waste; Activated carbon; Adsorption; Malachite green; Adsorption kinetic

1. Introduction

Adsorption is one of the most effective processes of advanced wastewater treatment that industries employ to reduce hazardous pollutants in effluents. Many textile industries use commercial activated carbon (AC) for the treatment of dye waste. AC is a carbonaceous material known for its large specific surface area, well-built pore structure, high physicochemical stability, and excellent surface reactivity, and it is widely employed as a functional material for various applications. The global AC demand was 12,804,000 tons in 2015 and is expected to grow owing to stricter environmental regulations regarding water resources, clean gas application, and air quality control [1]. However, there are some issues related to AC production regarding its sustainability and availability owing to the usage of conventional precursors, such as coal, pitches, coke, and feeds, which are non-renewable, depleting, intensively generated, and consequently

* Corresponding author.

† This author is equally contributed and should be considered as co-first author.

affect the economic feasibility of the product [2]. Hence, many studies have been conducted to produce cheap and efficient AC from low-cost and renewable resources, such as oak wood [3], coconut pitch [4], walnut wood [5], rice straw [6], grape pomace [7], pomelo peel [8], mussel shell [9], sawdust [10], oil palm waste [11], orange peel [12], and cotton waste [13,14]. Most of the studies have focused on agricultural waste due to its abundant availability.

This study focused on less explored gasification waste (GW) as an AC precursor. It is estimated that the gasification market reached US $78 billion in 2017 and an increasing trend up to the US $126 billion is anticipated by 2023 [15]. The growth of the gasification market means a significant increase in gasification char (GC) disposal, which can be potentially used as a precursor for AC production. To date, there are few reports regarding its application in dye adsorption [16,17]. For example, Maneerung et al. [18] studied gasification residues as an AC precursor for rhodamine B adsorption. Other studies have utilized GC for heavy metal and tar removal as well as other applications, such as soil amendment and catalysts.

The use of malachite green (MG) for any aquatic species is not approved by the FDA or the U.S. Environmental Protection Agency [19]. However, it is still being used as an antiparasitic and antifungal agent in aquacultures because stakeholders are unaware of the potential genotoxic and carcinogenic properties of MG, and in addition, MG is relatively inexpensive, readily available, and highly efficacious [20]. To date, there have been no reported studies on MG removal using carbon residues from biomass gasification plants.

In this study, GC residues from woodchip gasification were used as an AC precursor to study the MG adsorption for batch and continuous operations. The economic feasibility of the AC is discussed in this paper. For kinetic, equilibrium, and column analysis, non-linear forms of the models were applied for the analysis of the experimental adsorption data to minimize the error and to predict the trend. The non-linear isotherm models such as Fritz–Schlünder and *n*-BET (Brunauer–Emmett–Teller) were used in this study as the application of these models is scarcely found in the literature.

2. Materials and methods

2.1. Materials

2.1.1. Precursor preparation and physiochemical activation

GW was collected from a local commercial gasification plant at Kuang, Selangor, Malaysia. The sample was washed, dried in an oven at 105°C for 24 h, sieved to the size of 0.5–1 mm and treated with potassium hydroxide (KOH) at various impregnation ratios (IR), as calculated by:

$$\mathrm{IR} = \frac{w_{\mathrm{KOH}}}{w_{\mathrm{char}}} \tag{1}$$

where w_{KOH} (g) is the dry weight of the KOH pellets, and w_{char} (g) is the dry weight of the GW. Deionized water was then added to dissolve all the KOH pellets. The sample was dried in the oven overnight at 105°C for 24 h. Microwave-induced activation of the impregnated char was conducted at different powers (264, 440, and 616 W) and at different radiation times (1, 4.5, and 8 min) with a continuous flow of CO_2 gas at 150 cm^3 min^{-1} using a conventional 2.45 GHz microwave oven that was modified to accommodate the reactor and the inlet and outlet of the gases. The activated product was then cooled to room temperature under nitrogen flow. Then, the sample was rinsed with deionized water and HCl (0.1 M) to reach pH 7. The obtained gasification waste-based activated carbon (GWAC) was dried at 110°C for 24 h.

2.2. Characterization methods

Nitrogen adsorption–desorption measurements (Model: Micromeritics ASAP 2020, USA) were performed to determine the BET surface area, Barrett–Joyner–Halenda pore size distribution (PSD), total pore volume (TPV), and average pore diameter (APD) of the sample. The surface morphology of the samples was examined via scanning electron microscopy (SEM) (Model: LEO SUPRA 55VP, Germany). Fourier-transform infrared spectroscopy (FTIR) (Model: Shimadzu Prestige 21, Japan) spectroscopy was used to evaluate the chemical structural properties. The proximate analysis was analyzed using thermogravimetric analysis equipment (Model: Perkin Elmer STA 6000, USA), while elemental analysis was conducted using a CHONS analyzer (Model: Perkin Elmer Series II 2400, USA).

2.3. Experimental design

Standard response surface methodology with the central composite design was used to optimize the GWAC preparation conditions based on the obtained MG removal efficiency and yield. There were three variables used, including radiation power (*A*), activation time (*B*), and impregnation ratio (*C*), as shown in Table 1. A total of 20 experiments were performed for the three factors, which consisted of 14 experiments plus 6 replicate parameters to evaluate the error. The corresponding model is a quadratic model expressed by Eq. (2):

$$Y = b_0 + \sum_{i=1}^{n} b_i x_i + \sum_{i=1}^{n} b_{ii} x_i^2 + \sum_{i=1}^{n-1} \sum_{j=i+1}^{n} b_{ij} x_i x_j + e_i \tag{2}$$

where Y is the predicted response, b_0 is the constant coefficient, b_i is the linear coefficient, b_{ij} is the interaction coefficient, b_{ii} is the quadratic coefficient, x_i and x_j are the coded values of the GWAC preparation variables, and e_i is the error. Design-Expert Software (version 6.0.7) was used to analyze the regression, variance (ANOVA), and response surfaces.

The adsorption process was conducted in a water bath shaker using a 250 mL conical flask at an initial MG concentration, GWAC dosage, shaker speed, and temperature of 100 mg L^{-1}, 0.2 g, 150 rpm, and 30°C, respectively.

2.4. Equilibrium and kinetic studies

The adsorption of MG was conducted at various initial MG concentrations (50–300 mg L^{-1}) at different temperatures (30°C, 45°C, and 60°C) using a water bath shaker for 24 h. For each test, GWAC with a mass of 0.2 g was added to a 200 mL MG solution. The experimental points were examined using isotherm models as listed in Table 2.

Table 1
Experimental variables and levels

Variable	Code	Coded values		
		–1	0	1
Radiation power, W	x_1	264	440	616
Radiation time, min	x_2	1	4.5	8
Impregnation ratio (IR), g g^{-1}	x_3	0.5	1.25	2

The kinetic studies followed the same steps for the desired contact time ranging from 15 to 1,440 min. The models that were used to evaluate the effect of contact time on the MG adsorption are shown in Table 3.

The equilibrium and kinetic studies were performed using the curve fitting tools provided in Matlab R2019b. The error functions that were used to optimize the model are listed in Table 4.

2.5. Thermodynamic study

The thermodynamics parameters of MG adsorption were studied by applying the Van't Hoff equation [35]:

$$\ln K_c = \frac{\Delta S^\circ}{R} - \frac{\Delta H^\circ}{RT} \tag{3}$$

where K_c is the equilibrium constant (dimensionless), ΔG° (kJ mol^{-1}) is the Gibbs energy change, ΔH° (kJ mol^{-1}) is the enthalpy change, ΔS° (kJ mol^{-1} K^{-1}) is the entropy change, and R (8.314 J mol^{-1} K^{-1}) is the universal gas constant.

The standard free energy change was calculated by:

$$\Delta G^\circ = \Delta H^\circ - T\Delta S^\circ \tag{4}$$

$$\Delta G^\circ = -RT\ln\left(K_c\right) \tag{5}$$

Table 2
Non-linear equilibrium models

Isotherm	Equation	Parameter	Reference
Freundlich	$q_e = K_F C_e^{1/n}$	K_F, $1/n$	[8]
Langmuir	$q_e = \frac{q_{\max} K_L C_e}{1 + K_L C_e}$	$q_{\max}$, K_L	[21]
Dubinin–Radushkevish (D–R)	$q_e = q_{DR}\exp\left[\frac{\left(RT\ln\left(1+1/C_e\right)\right)^2}{-2E^2}\right]$	q_{DR}, E	[22]
Temkin	$q_e = \frac{RT}{b_T}\ln\left(K_T C_e\right)$	b_T, K_T	[23]
Redlich–Peterson (R–P)	$q_e = \frac{K_R C_e}{1 + A_R C_e^{\alpha_{RP}}}$	K_R, A_R, α_{RP}	[24]
Sips	$q_e = \frac{q_S K_S C_e^{n_S}}{1 + K_S C_e^{n_S}}$	q_S, K_S, n_S	[25]
Koble–Corrigan (K–C)	$q_e = \frac{A_{KC} C_e^{k_{KC}}}{1 + B_{KC} C_e^{k_{KC}}}$	A_{KC}, B_{KC}, k_{KC}	[26]
Fritz–Schlünder (F–S)	$q_e = \frac{AC_e^{\alpha}}{1 + BC_e^{\beta}}$	A, B, α, β	[27]
n-layer BET	$q_e = q_m \frac{K_S C_e\left[1-\left(n_{BET}+1\right)\left(K_{L_{BET}} C_e\right)^{n_{BET}} + n_{BET}\left(K_{L_{BET}} C_e\right)^{n_{BET}+1}\right]}{\left(1-K_{L_{BET}} C_e\right)\left[1+\left(\frac{K_S}{K_{L_{BET}}}-1\right)K_L C_e - \left(\frac{K_S}{K_{L_{BET}}}\right)\left(K_{L_{BET}} C_e\right)^{n_{BET}+1}\right]}$	q_m, K_S, K_{LBET}, n_{BET}	[28]
Toth	$q_e = \frac{q_{m_{Toth}} k_{Toth} C_e}{\left[1+\left(k_{Toth} C_e\right)^{n_{Toth}}\right]^{1/n_{Toth}}}$	q_{mToth}, k_{Toth}, n_{Toth}	[29]

Table 3
Non-linear kinetic models

Isotherm	Equation	Parameter	Reference
Pseudo-first-order	$q_t = q_e\left[1-\exp\left(-k_1 t\right)\right]$	q_e, k_1	[30]
Pseudo-second-order	$q_t = \frac{k_2 q_e^2 t}{1+k_2 q_e t}$	q_e, k_2	[31]
Elovich	$q_t = \frac{1}{\beta}\ln\left(\alpha_E \beta\right)+\frac{1}{\beta}\ln\left(t\right)$	α_E, β	[32]
Avrami	$q_t = q_e\left\{1-\exp\left[-\left(k_{\mathrm{AV}} t\right)\right]^{n_{\mathrm{AV}}}\right\}$	q_e, k_{AV}, n_{AV}	[33]
Weber–Morris intraparticle diffusion	$q_t = k_{\mathrm{WM}}\sqrt{t}+C$	k_{WM}, C	[34]

Table 4
Error functions and their expressions

Error function	Abbreviation	Expression
Coefficient of determination	R^2	$1-\frac{\sum_{i=1}^{n}\left(q_{e,\exp}-q_{e,\mathrm{calc}}\right)^2}{\sum_{i=1}^{n}\left(q_{e,\exp}-\bar{q}_{e,}\right)^2}$
Chi square	χ^2	$\sum_{i=1}^{N}\frac{\left(q_{e,\exp}-q_{e,\mathrm{calc}}\right)^2}{q_{e,\mathrm{calc}}}$
Sum of squares errors	SSE	$\sum_{i=1}^{N}\left(q_{e,\exp}-q_{e,\mathrm{calc}}\right)^2$
Root mean square error	RMSE	$\sqrt{\frac{1}{N-2}\times\sum_{i=1}^{N}\left(q_{e,\exp}-q_{e,\mathrm{calc}}\right)^2}$
Average relative errors	% ARE	$\frac{100}{N}\sum_{i=1}^{n}\left\lvert\frac{\left(q_{e,\exp}-q_{e,\mathrm{calc}}\right)}{q_{e,\exp}}\right\rvert$

The thermodynamic equilibrium constant was approximated by the Langmuir constant (K_L) or the equilibrium constant of the monolayer (K_S) [36,37]. This simplification is only valid for dilute solutions, such as dyes molecules [38,39].

2.6. Fixed-bed column study

The adsorption of MG was evaluated in continuous adsorption mode using a 14-mm inner diameter glass tube with a length of 100 mm with different bed heights (10, 20, and 30 mm). An MG solution with an initial concentration of 100 mg L^{-1} was pumped upward through the column at the desired flow rate using a peristaltic pump (0.5, 1, and 2 mL min^{-1}). Samples were gathered from the exit of the column, and the column was stopped when the saturation state was reached (C_t/C_0 reached unity). The MG concentration in the effluent was determined using a UV-vis spectrophotometer.

For the analysis of the experimental breakthrough curves, the Thomas (Eq. (7)) [21], Yoon–Nelson (Eq. (8)) [40], and Bohart–Adams (Eq. (9)) [41] models were used:

$$\left(\frac{C_t}{C_0}\right)=\frac{1}{1+\exp\left(k_{\mathrm{TH}} q_0 \frac{m}{Q}-k_{\mathrm{TH}} C_0 t\right)} \tag{7}$$

$$\left(\frac{C_t}{C_0}\right)=\frac{1}{1+\exp\left[k_{\mathrm{YN}}\left(\tau-t\right)\right]} \tag{8}$$

$$\left(\frac{C_t}{C_0}\right)=\exp\left(k_{\mathrm{BA}} C_0 t-\frac{k_{\mathrm{BA}} N_0 H}{v}\right) \tag{9}$$

where k_{TH} (mL mg^{-1} h^{-1}) is the Thomas kinetic constant, q_0 (mg g^{-1}) is the maximum capacity of the sorbent, Q (mL h^{-1}) is the volumetric flow rate, m (g) is the mass of the adsorbent used, C_0 (mg mL^{-1}) is the initial adsorbate concentration, k_{YN} (h^{-1}) is the Yoon–Nelson kinetic constant, τ (h) is the contact time required for 50% breakthrough of the adsorbate, k_{BA} (mL mg^{-1} h^{-1}) is the Bohart–Adams constant, N_0 (mg L^{-1}) is the saturation concentration, H (cm) is the bed height, and v (cm min^{-1}) is the linear flow rate.

3. Results and discussion

3.1. Experimental results

Table 5 shows the experimental results obtained for the two investigated responses. For both responses, the quadratic model was selected, and the final empirical formulas for MG removal (Y_1) and GWAC yield (Y_2) in terms of the coded factors were given by Eqs. (10)–(11).

$$Y_1 = 94.53 + 7.16x_1 + 6.70x_2 + 8.16x_3 - 6.53x_1x_3 - 7.41x_2x_3 \quad (10)$$

$$Y_2 = 84.86 - 1.76x_1 - 4.09x_2 + 2.67x_2^2 \quad (11)$$

The R^2 values from Eqs. (10) and (11) were 0.8263 and 0.9204, respectively, indicating the predicted value for MG removal and GWAC yield were acceptable and reasonably match the real value. High IR, radiation power, and time resulted in better MG removal but reduced the yield of GWAC. Thus, an optimal solution is needed to compromise both responses.

The ANOVA result from the quadratic model corresponding to the MG removal and GWAC yield are shown in Tables 6 and 7. The model was significant if the *F*-value was larger with a smaller *P*-value or *P*-value of <0.05 [42,43].

The Prob. > *F* of less than 0.05 shows that both models were significant. As shown in Table 6, the model terms of X_1 (radiation power), X_2 (radiation power), X_3 (IR), X_1X_3, and X_2X_3 were significant to the response. The lack of a fit *P*-value of 0.0754 was not significant, and the regression model was effective for MG adsorption onto GWAC. As shown in Table 7, X_1, X_2, X_3, X X_3 and X_2, X_3 were significant model terms with a lack of fit that were insignificant to the response.

Fig. 1a shows the surface plot for the effects of radiation power and IR on MG removal. MG removal increased with the radiation power and IR as more pores and surface area developed, which could be occupied by MG molecules. Increasing the radiation power widened the existing pores and formed new pores via a continual carbon–CO_2 reaction of the carbon burn off, resulting in an increasing BET surface area [44].

Fig. 1b shows a surface plot of the effect of radiation power and time on the GWAC yield. The yield of GWAC produced was inversely proportional to the microwave power and irradiation time, and a lower yield was obtained at higher microwave powers and longer irradiation times. This was due to the release of more volatile matter during the activation stage at higher microwave powers and

Table 5
Experimental results of the responses

Run	Factor 1	Factor 2	Factor 3	Response 1	Response 2
	A: Power	*B*: Time	*C*: IR ratio	MG removal	GWAC yield
1	616	1.00	2.00	99.90	90.53
2	264	8.00	0.50	90.63	85.19
3	616	8.00	0.50	98.67	82.38
4	616	8.00	2.00	99.99	82.94
5	440	4.50	0.50	85.53	85.76
6	616	4.50	1.25	92.95	85.03
7	264	8.00	2.00	95.70	86.01
8	616	1.00	0.50	90.41	89.89
9	440	4.50	1.25	96.78	85.65
10	264	1.00	2.00	93.56	95.89
11	440	4.50	1.25	95.90	83.32
12	264	4.50	1.25	92.89	86.24
13	440	4.50	1.25	90.89	86.20
14	440	1.00	1.25	94.69	90.60
15	440	4.50	1.25	96.76	82.12
16	440	4.50	1.25	85.76	85.42
17	264	1.00	0.50	36.59	95.06
18	440	4.50	2.00	95.22	84.57
19	440	8.00	1.25	96.31	84.57
20	440	4.50	1.25	98.99	86.23

Table 6
ANOVA results for MG removal

Source	Sum of squares	Degree of freedom	Mean square	*F*-value	*P*-value Prob. > *F*
Model	2,855.27	9	317.25	5.18	0.0085
x_1	512.08	1	512.08	8.36	0.0161
x_2	448.36	1	448.36	7.32	0.0221
x_3	665.04	1	665.04	10.86	0.0081
x_1x_2	276.36	1	276.36	4.51	0.0596
x_1x_3	340.87	1	340.87	5.56	0.0400
x_2x_3	438.97	1	438.97	7.17	0.0232
x_1^2	12.41	1	12.41	0.20	0.6622
x_2^2	0.57	1	0.57	0.01	0.9250
x_3^2	59.96	1	59.96	0.98	0.3458
Residual	612.63	10	61.26		612.63
Lack of fit	491.40	5	98.28	4.05	0.0754
Pure error	121.23	5	24.25		
Cor. total	3,467.90	19			

Table 7
ANOVA results for GWAC yield

Source	Sum of squares	Degree of freedom	Mean square	*F*-value	*P*-value Prob. > *F*
Model	256.34	9	28.48	12.84	0.0002
x_1	31.05	1	31.05	14.00	0.0038
x_2	167.12	1	167.12	75.34	<0.0001
x_3	0.28	1	0.28	0.12	0.7318
x_1x_2	2.70	1	2.70	1.22	0.2955
x_1x_3	0.03	1	0.03	0.01	0.9170
x_2x_3	0.00	1	0.00	0.00	0.9834
x_1^2	1.43	1	1.43	0.64	0.4414
x_2^2	19.60	1	19.60	8.84	0.0140
x_3^2	0.17	1	0.17	0.08	0.7864
Residual	22.18	10	2.22		
Lack of fit	7.70	5	1.54	0.53	0.7475
Pure error	14.48	5	2.90		
Cor. total	278.52	19			

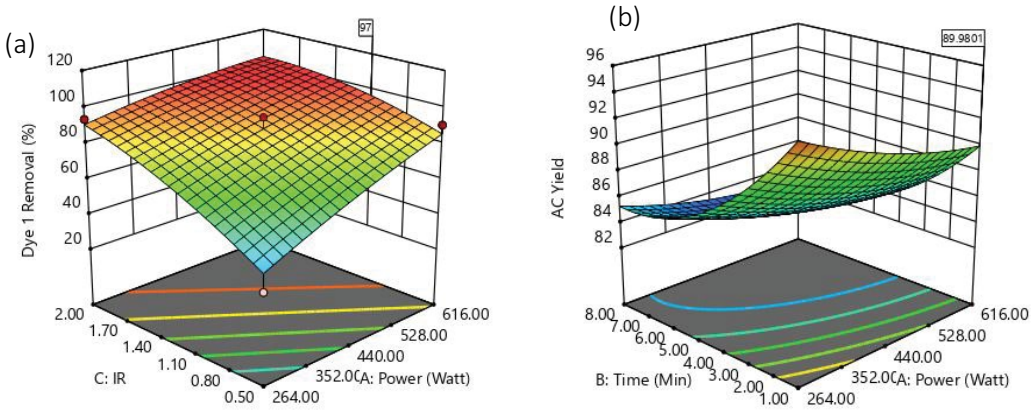

Fig. 1. (a) Effect of IR and power on MG removal and (b) effect of power and time on the GWAC yield.

longer irradiation times. The carbon elements present in the sample absorbed more microwave energy, thus inducing dipole rotation of carbon molecules at the rate of a million times per second [45]. This rapid rotation of carbon molecules within the char thus produced frictional force and released more heat energy within the char itself, which thus improved the pyrolysis cracking of the GW and released more volatile matter. As a result, lower GWAC yield was obtained owing to the release of a higher amount of volatile matter from the sample. This finding was in agreement with those reported by Lam et al. [46] and Ahmad et al. [47], who also synthesized AC using a microwave irradiation technique.

The optimum conditions for synthesizing GWAC are summarized in Table 8. The optimum conditions for GWAC were achieved at a high radiation power with minimum IR and activation time. In contrast, other researchers reported high radiation power and time for efficient removal of the MG dye.

3.2. N_2 adsorption isotherms, PSD, and physical properties

The N_2 adsorption–desorption isotherms for GW and GWAC are shown in Fig. 2a. Both GW and GWAC exhibited a combination of Type I and II isotherms [51], which exhibited micro- and mesoporous structures. A similar trend was reported by Ogungbenro et al. [52], Lam et al. [50], Yang and Hong [53], and Foo and Hameed [54] using AC from date seed, orange peel, *Glossogyne tenuifolia* leaves, and pineapple peel, respectively.

As shown in Table 9, raw GW possessed a relatively low BET surface area and a TPV of 257.96 $m^2\ g^{-1}$ and 0.1605 $cm^3\ g^{-1}$, respectively. After the activation step, the surface area and TPV increased owing to pore development and widening of the existing pores [55]. The increase in TPV was verified by the increase in adsorption at low relative pressures ($p/p_0 < 0.1$), as depicted in Fig. 2a. A similar trend was reported by Pallarés et al. [56], who studied the characterization of AC from barley straw. The APD of GWAC was 3.4932 nm, which indicated that the pore structure of GWAC can ideally accommodate the MG dye that has molecular dimensions of 1.21 nm × 1.19 nm × 0.53 nm [57].

3.3. Proximate and elemental analysis

Fig. 3 indicates the proximate and elemental analysis results of GW and GWAC. In general, the produced GWAC has closely followed the AC standard in SNI-06-3730-1995 [58]. There is a slight decrease in fixed carbon composition after the activation process due to high irradiation power used that caused the breakdown of AC structures [59], as well as high IR value which can damage the micropore on the carbon surface. The moisture content of GWAC increases due to water formation at high temperatures resulting from dehydration reactions of close carboxylic groups and phenyl groups to anhydrides, lactones, and ether [60]. Besides, high IR value increases the amount and volume of pores and surface area, which causes an increase in the performance of AC to absorb water from the air [61]. An increasing trend for volatile matter composition was also reported

Table 8
Optimal activation conditions for GWAC synthesis

Type of AC	Power (W)	Time (min)	IR	Yield (%)	Actual MG removal (%)	Reference
GWAC	616	1	1.06	89.98	99.01	This study
Banana peel	700	10	1.00	29	90.00	[45]
Ricinus communis	100	4	0.30	69.68	55.6–88.24	[48]
Casuarina equisetifolia seeds	800	8	2.00	n/a	95.95	[49]
Orange peel	550	5	1.00	87.00	57.00	[50]

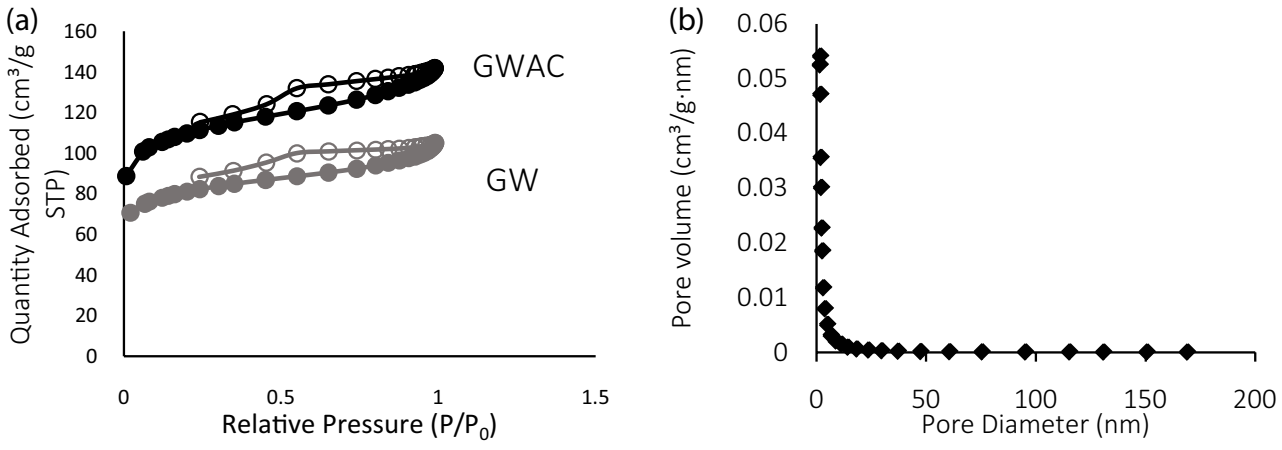

Fig. 2. (a) N_2 adsorption–desorption isotherms of GW and GWAC and (b) PSD of GWAC.

Table 9
Physical properties of GW and GWAC

	S_{BET} (m^2 g^{-1})	TPV (cm^3 g^{-1})	V_{micro} (cm^3 g^{-1})	APD (nm)	% V_{micro}	S_{micro}/S_{BET}
GW	257.9607	0.1605	0.0875	3.5729	54.5509	66.5285
GWAC	351.9315	0.2174	0.1175	3.4932	54.0496	66.1511

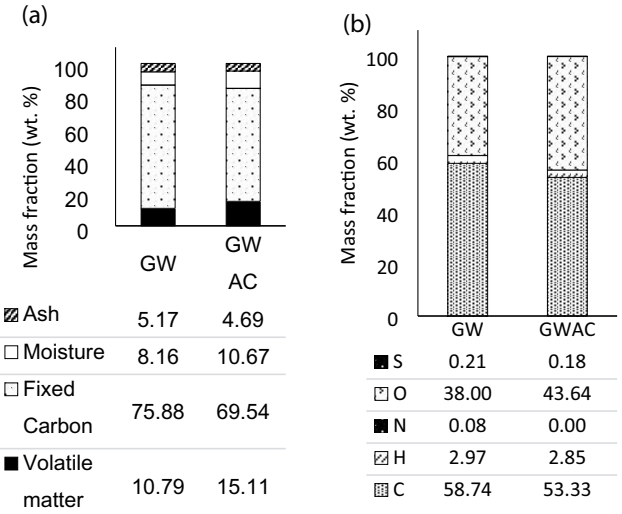

Fig. 3. (a) Proximate analysis of GW and GWAC and (b) elemental analysis of GW and GWAC.

by Yang and Qiu [62], who synthesized AC from herb residue using $ZnCl_2$. KOH-CO_2 modification reduced the ash in GWAC which was confirmed by the declining value of ash content from 5.17 to 4.69% after modification.

3.4. Sample morphology

The surface morphology details of the samples were determined by SEM for further comparison of the porosity. Fig. 4a illustrates the morphology of GW, whereas Fig. 4b shows the GWAC structure. Generally, GW exhibited abundant honeycomb pore structures because most of the volatile compounds were released during the gasification process. After KOH-CO_2 activation, clearly, the cylindrical porous structure became wider, and new slit-shaped pores formed. This pore structure provides channels for molecules of the adsorbate to move into the cavities of the carbon surface. A similar honeycomb structure was observed by Khadhri et al. [63], who characterized AC derived from date palm petiole.

3.4.1. Sample functional groups

The FTIR spectra are shown in Fig. 5 reveal multiple types of functional groups on the surface of GW. Carbonyl, ether, ester, alcohol, and phenol groups are the main oxygen groups present in GW. However, most of the functional groups disappeared after activation. The broad peak from 3,700 to 3,100 cm^{-1} was assigned to –OH stretching in the phenolic and aliphatic structures of the remaining cellulose, hemicellulose, and lignin in GWAC [64]. The spectral region of 2,420–2,268 cm^{-1} is attributed to an alkyne group (C≡C) and remained in GWAC after the activation process [65,66]. The absorption at approximately 1,600 cm^{-1} is attributed to highly conjugated carbonyls (quinone groups) and C=C stretching vibrations in the aromatic ring [67,68]. The peaks at 1,419–1,411 cm^{-1} indicate C–H symmetrical bending from methyl groups or the –CH_2 scissoring vibration, which disappeared in the IR spectrum of GWAC, demonstrating a decrease in C–H bonds in favor of aromatization [69,70]. Similar results have been reported by Mosley et al. [72] and Zhang et al. [73]. In conclusion, the FTIR

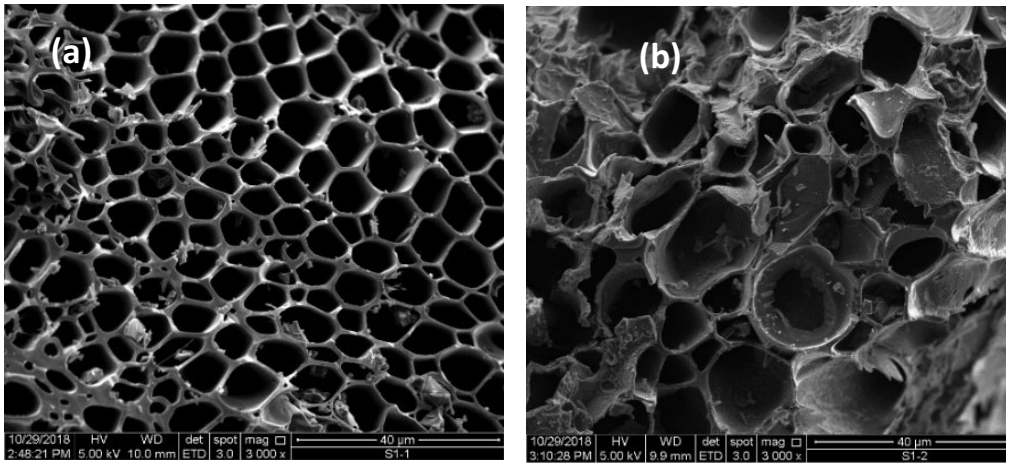

Fig. 4. SEM images of (a) GW and (b) GWAC.

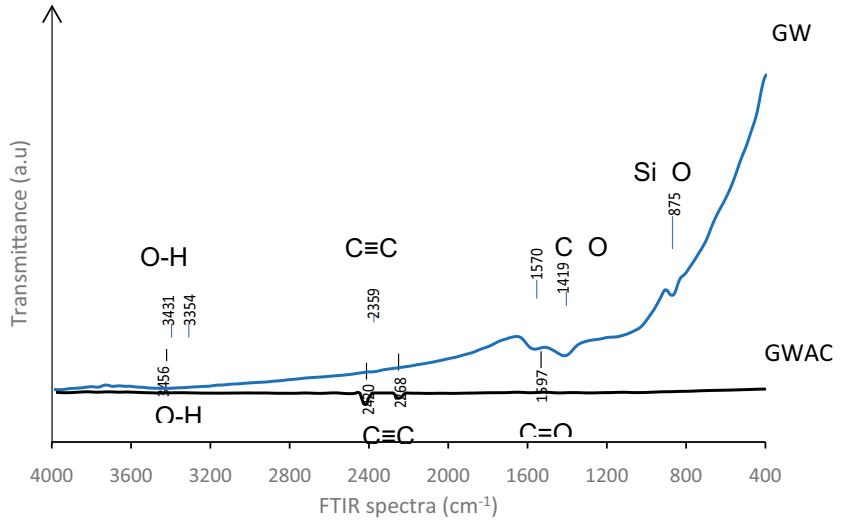

Fig. 5. FTIR spectra of GW and GWAC.

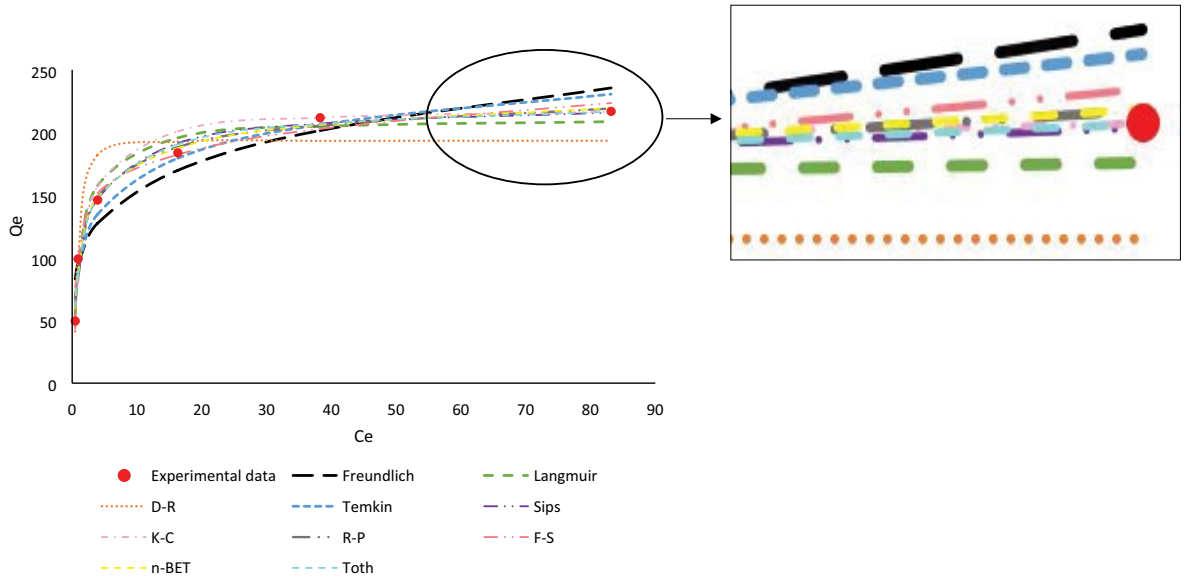

Fig. 6. Fitting of equilibrium data using various isotherm models.

results suggested that the surface functional groups and the structure of GWAC changed significantly, which were mainly due to carbon-CO_2 and carbon-KOH reactions [74].

3.5. Equilibrium and kinetic studies

3.5.1. Equilibrium models

As shown in Table 10, the Fritz–Schlünder isotherm was the one that fit best to the equilibrium data for all studied temperatures. The Fritz–Schlünder isotherm model is for four parameters and a combination of Langmuir and Freundlich isotherms. Based on the error functions indicated in Table 10, the Langmuir isotherm model fits better than the Freundlich isotherm model. An n_F value of 0.2, which was between 0 and 1, indicates a favorable adsorption isotherm.

The relatively high value of the regression coefficient, R^2, obtained in the nth layer BET (multilayer model) confirmed its applicability for describing the experimental data. The values of n_{BET} (number of layers formed) were below 1.5, which can be considered to represent monolayer adsorption. However, there is a probability that the adsorption of MG predominantly occurred on the first GWAC layers; regardless, the possibility of multilayer sorption, although to a lower extend, could not be neglected.

The 3-parameter isotherm models, Redlich–Peterson, Toth, and Sips were also applicable to predict the equilibrium behavior of MG adsorption with high R^2 values.

Table 10
Non-linear isotherm parameters

Model	Parameter	Temperature (°C)		
		30	45	60
Freundlich	K_F ($mg^{1-1/n}L^{1/n}g^{-1}$)	96.93	105.1	109.2
	n	4.98	5.285	5.305
	R^2	0.9036	0.8921	0.8832
	χ^2	19.5227	22.6050	24.9427
	SSE	2,130	2,525	2,864
Langmuir	K_L (L mg^{-1})	0.7356	1.029	1.055
	q_{max} (mg g^{-1})	212	215	220.5
	R^2	0.9721	0.9638	0.9744
	χ^2	4.9400	7.8102	5.9010
	SSE	617.6	848.2	628.3
Dubinin–Radushkevish (D–R)	q_{DR} (mg g^{-1})	193.4	197.9	202
	E (kJ mol^{-1})	0.6058	0.4652	0.4398
	R^2	0.894	0.8959	0.9042
	χ^2	13.8678	13.0968	12.6167
	SSE	2,342	2,436	2,349
Temkin	b_T (J mol^{-1})	0.08031	0.08692	0.08856
	K_T (L mg^{-1})	18.64	30.02	30.86
	R^2	0.9636	0.954	0.9513
	χ^2	8.1024	10.8844	11.3623
	SSE	803.9	1,076	1,194
Redlich–Peterson (R–P)	K_R (L g^{-1})	208.5	298.1	296.8
	A_R (L mg^{-1})	1.258	1.743	1.626
	α_{RP}	0.934	0.936	0.9464
	R^2	0.9862	0.9804	0.9858
	χ^2	3.5779	5.8015	4.5766
	SSE	304.3	457.9	348.7
Sips	q_S (mg g^{-1})	228.2	232.4	233.1
	K_S (L mg^{-1})	0.6524	0.8233	0.8912
	n_S	0.7431	0.7206	0.7781
	R^2	0.9822	0.977	0.9827
	χ^2	4.6945	6.9746	5.5670
	SSE	393.5	539.2	425.1
Koble–Corrigan (K–C)	A_{KC} (L g^{-1})	138.2	182.6	195.7
	B_{KC} (L mg^{-1})	0.6265	0.8182	0.8667
	k_{KC}	1	1	1
	R^2	0.9644	0.9541	0.9678
	χ^2	6.9368	12.2880	9.3562
	SSE	787.1	1073	790.1
Fritz–Schlünder (F–S)	A (L g^{-1})	128.6	135.5	141.8
	B (L mg^{-1})	0.234	0.04964	0.08194
	α	0.125	0.1201	0.115
	β	–2.568	–3.177	–2.568
	R^2	0.9932	0.9920	0.9919
	χ^2	1.7253	0.9698	1.0832
	SSE	151.2	187.9	348.9

(Continued)

Table 10 Continued

Model	Parameter	Temperature (°C)		
		30	45	60
n-layer BET	q_{maxBET} (mg g^{-1})	163.5	169.4	172.1
	K_{LBET} (L mg^{-1})	0.036	0.0613	0.06293
	K_S (L mg^{-1})	1.204	1.777	1.66
	n_{BET}	1.488	1.502	1.419
	R^2	0.9874	0.9816	0.9865
	χ^2	3.3671	8.0783	4.4358
	SSE	279.5	430	331.8
Toth	q_{maxT} (mg g^{-1})	257.2	306.1	279.6
	k_{Toth} (L mg^{-1})	1.195	1.53	1.449
	n_{Toth}	0.6444	0.6243	0.69
	R^2	0.9838	0.9788	0.984
	χ^2	4.3054	6.5539	5.2089
	SSE	358.2	504.3	392.8

The constant values from these models (α_{RP}, n_{Toth}, and n_s), which were close to 1 delineated the homogeneous binding sites on the GWAC surface. The low adsorption energy, E (<8 kJ mol^{-1}), indicated physisorption. In relation to the Temkin adsorption isotherm, the increased value of b_T revealed that the adsorption was endothermic.

Additionally, the lower values of b_T (<20 kJ mol^{-1}) indicated the characteristics of physisorption. Similar findings were reported by Kim and Kim [74] and Soltani et al. [75]. The experimental and predicted equilibrium plots are shown in Fig. 5. The following show the ranking of the isotherm model in descending order (best to poorest fitting) with respect to R^2 and the sum of squares errors value Fritz–Schlünder > n^{th} layer BET > Redlich–Peterson > Toth > Sips > Langmuir, Koble–Corrigan > Temkin > Freundlich > Dubinin–Radushkevish, and with respect to χ^2 value, the order is Fritz–Schlünder > n^{th} layer BET > Redlich–Peterson > Toth > Sips > Langmuir, Koble–Corrigan > Temkin > Dubinin–Radushkevish > Freundlich.

3.5.2. Kinetic models

Table 11 presents the kinetic constants obtained by fitting the kinetic data via non-linear regression analysis, and their corresponding non-linear curves are shown in Fig. 7. The results of these fittings show that rapid adsorption occurred over 30 min, and equilibrium was reached after 6 h, indicating that the adsorbent surface and adsorbate molecules interacted favorably. Among the five kinetic models, the pseudo-first-order equation provided the best correlation between experimental data with low root mean square error values. The kinetics of MG adsorption on the GWAC surface can be described by the following descending order of fitting: pseudo-first-order > Avrami > pseudo-second-order > Elovich and intraparticle diffusion models. The calculated equilibrium adsorption capacity agreed very well with the experimental equilibrium adsorption capacity.

The intraparticle diffusion model was used to identify the adsorption mechanism. As shown in Fig. 7d, the plots were not linear over the whole-time range and did not pass through the origin. This indicated that the intra-particle diffusion was not the only rate-limiting step. There are two major phases in the plot; the initial steep phase is related to rapid diffusion across the external boundary layer to the surface of the GWAC, and the second phase that has a gradual slope corresponds to diffusion through the pores of the adsorbent. This finding suggests that both surface adsorption and intraparticle diffusion mechanisms are involved in MG adsorption [76,77].

3.6. Mechanism of MG adsorption

3.6.1. Boyd's plot

Since intraparticle diffusion was not the only rate-limiting step in this adsorption process, Boyd's plot was further constructed to confirm whether the adsorption was governed by film diffusion. Fig. 8 illustrates Boyd's plot of MG adsorption on GWAC.

Although the plot shows the linear relation between b_T and t, it however does not pass through the origin, confirming the surface diffusion is the rate-limiting step for the adsorption process.

3.6.2. Evaluation of pH_{PZC} and effect of pH on MG adsorption

Fig. 9 shows the plot of MG adsorption capacity against initial solution pH and the value of pH_{pzc}. The equilibrium uptake of MG significantly increased with the increase of pH from 2.0 to 4.0. Beyond pH 4.0, there was no significant change in the MG adsorption capacity. The reduced uptake of the MG below pH 4.0 was due to electrostatic repulsion between the positively charged surface of the adsorbent and the positively charged cationic MG dye.

The surface charge of the adsorbent can be determined by the point of zero charge (pH_{PZC}). The pH_{PZC} of GWAC

Table 11
Non-linear kinetic parameters

Model	Initial concentration (mg L^{-1})								
	100			200			300		
	Parameter	Temperature (°C)								
		30	45	60	30	45	60	30	45	60
Pseudo-first-order	q_e (mg g^{-1})	98.18	98.32	98.56	180.700	185.8	187.8	213.2	217.6	222.3
	k_1	0.05066	0.05953	0.06574	0.05389	0.05572	0.0588	0.08987	0.09422	0.09803
	R^2	0.9871	0.9774	0.9813	0.979	0.9769	0.9758	0.9679	0.9653	0.9625
	RMSE	1.7415	1.9359	1.5930	3.7729	3.8891	3.8505	3.1854	3.1584	3.5792
	χ^2	0.3017	0.3890	0.2729	0.9282	0.9604	0.8634	0.4307	0.4158	0.5246
Pseudo-second-order	q_e	102.6	102.1	102	188.200	193.2	195.1	218.5	222.7	227.4
	k_2	0.00088	0.00111	0.00129	0.00053	0.00054	0.00057	0.00096	0.00103	0.00108
	R^2	0.9436	0.9652	0.959	0.967	0.9673	0.9703	0.9398	0.9399	0.949
	RMSE	3.6415	2.4020	2.3595	4.665	4.6321	4.2670	4.3654	4.1611	3.6325
	χ^2	1.6376	0.6261	0.5839	1.2732	1.1863	1.0171	0.9302	0.8156	0.6037
Elovich	$\alpha_E \times 10^4$	1.104	10.02	26.6	4.089	7.854	12.88	106.4	121.4	138.7
	β	0.1379	0.1612	0.1708	0.079	0.08039	0.08212	0.08078	0.07951	0.07822
	R^2	0.6004	0.6155	0.5863	0.647	0.6284	0.635	0.4647	0.4142	0.3532
	RMSE	9.6904	7.9892	7.4976	15.3258	15.6139	14.9524	13.0164	12.9856	12.7591
	χ^2	10.4146	6.7567	5.8005	13.8107	13.7469	12.4198	7.6173	7.3487	6.8383
Avrami	q_e	98.18	98.33	98.56	180.700	185.8	187.8	213.2	217.6	222.3
	k_{AV}	0.5018	0.4588	0.1526	0.188	0.2197	0.6603	0.248	0.6337	0.3088
	n_{AV}	0.101	0.1297	0.4307	0.286	0.2536	0.08906	0.3623	0.1487	0.3175
	R^2	0.9871	0.9774	0.9813	0.979	0.9769	0.9758	0.9679	0.9653	0.9625
	RMSE	1.8471	2.0534	1.6897	4.0018	4.1250	4.0841	3.3787	3.3500	3.7963
	χ^2	0.3016	0.3892	0.2731	0.9276	0.9607	0.8631	0.4308	0.4157	0.5246
Weber–Morris intraparticle diffusion	k_{WM}	0.64	0.5467	0.4787	1.389	1.104	1.081	0.771	0.7456	0.7158
	C	79.9	82.98	85.1	141.3	154.6	157.7	192.7	198	203.6
	R^2	0.3259	0.3367	0.3153	0.3604	0.3475	0.3567	0.3512	0.3612	0.3611
	RMSE	12.5851	10.4925	9.6458	20.9795	20.6903	19.8513	14.3295	13.5612	12.7929
	χ^2	16.8015	11.3429	9.4264	25.5530	23.5513	21.3216	9.3348	8.15396	7.0675

was found at pH 6.2. At pH < pHpzc, the adsorbent surface becomes predominantly positively charged and tend to repel the cationic dye since the number of the negatively charged groups at the surface of the adsorbent decreased, while the positively charged groups increased. Hence the adsorption of the dye molecules to the surface of the adsorbent reduced as pH was decreased from 4 to 2 due to the presence of electrostatic repulsion. The adsorption of MG was favorable above pH 4 or when pH>pH_{PZC}, which can be attributed by electrostatic interaction between negatively charged GWAC surface and positively charged MG. This result proved that the interaction mechanism of MG adsorption involves electrostatic interaction between MG adsorbate and the surface of GWAC. A similar trend was reported by Murthy et al. [78] and Sharma et al. [79].

3.6.3. Possible mechanism of MG adsorption

As observed in FTIR analysis, the GWAC surface contains limited functional groups such as –COOH and –OH. H–bonding and π–π interactions could be considered as the possible interaction that aid the adsorption of MG onto GWAC. Based on the pH influence on MG uptakes, electrostatic interaction further enhances the MG adsorption when the pH was increased. Fig. 10 illustrates the probable interaction mechanism between MG molecules and GWAC.

3.7. Thermodynamic study

ΔG° explains the thermodynamic process of adsorption with regards to its spontaneity. The Δ*G* values for MG adsorption onto GWAC were found to be –35.10 (30°C), –37.86 (45°C), and –39.46 (60°C) kJ mol^{-1}, which indicate energetically favorable and spontaneous adsorption. With a positive Δ*H*° (9.183 kJ mol^{-1}), the adsorption process was determined to be endothermic in nature. This study also revealed that the adsorption process of MG onto GWAC shows a linear plot of lnK_c vs. 1/*T* with increasing q_e as temperature increased as shown in Fig. 11. The Δ*S* of 146.65 J mol^{-1} showed an increase in unpredictability at the solid/liquid interface during the batch adsorption [80].

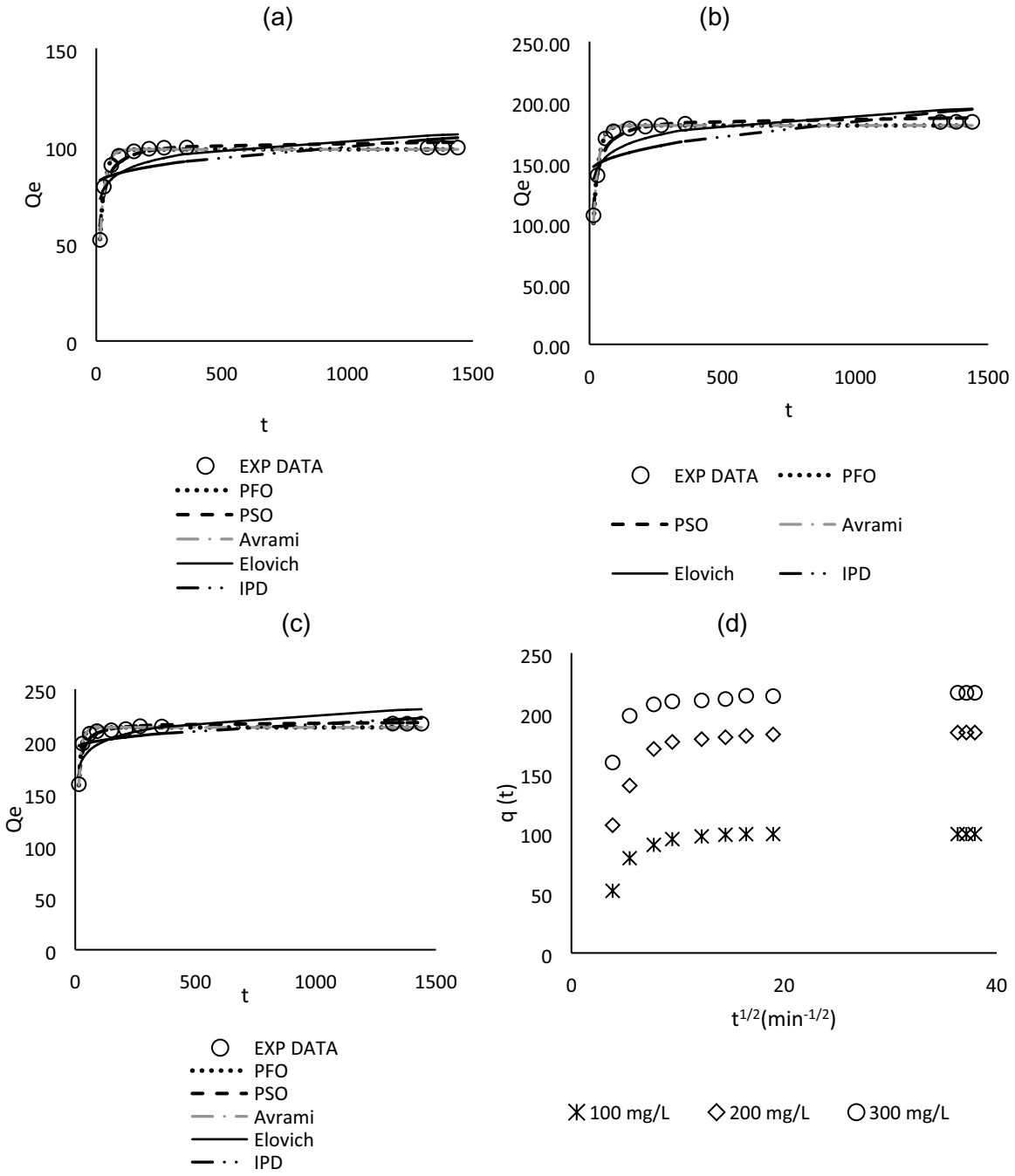

Fig. 7. Non-linear kinetic model plots for MG adsorption at 30°C and at different initial dye concentrations of (a) C_0 = 100, (b) C_0 = 200, (c) C_0 = 300 mg L^{-1}, and (d) the intraparticle diffusion model.

3.8. Breakthrough column study

The breakthrough curves and obtained results from the application of the Thomas, Yoon–Nelson, and Bohart–Adams models are presented in Fig. 12 and Table 12, respectively.

The effect of the flow rate on the adsorption rate constant was studied to confirm the dependence of mass transfer on the flow rate. As shown in Table 12, the rate constant, k_{TH}, increased from 1.899 to 8.383 mL mg^{-1} h^{-1} with increasing flow rate from 0.5 to 2 mL min^{-1}, which indicated that the mass transfer was controlled by flow rate. The adsorption capacity, q_0, was found to decrease with increasing flow rate. At a lower flow rate, the residence time of the adsorbate was longer; hence, the adsorbent had enough time for diffusion into the porous system of GWAC. In contrast, at a higher flow rate, the adsorption capacity was lower owing to the insufficient residence time, and the solute left the column before equilibrium occurred.

Fig. 12b shows that the breakthrough time was enhanced with increasing bed height owing to the availability of

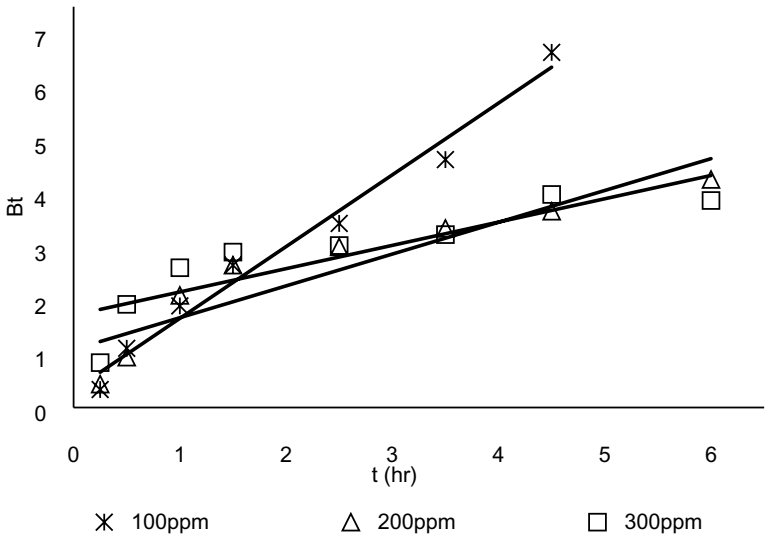

Fig. 8. Boyd's plot of MG adsorption on GWAC.

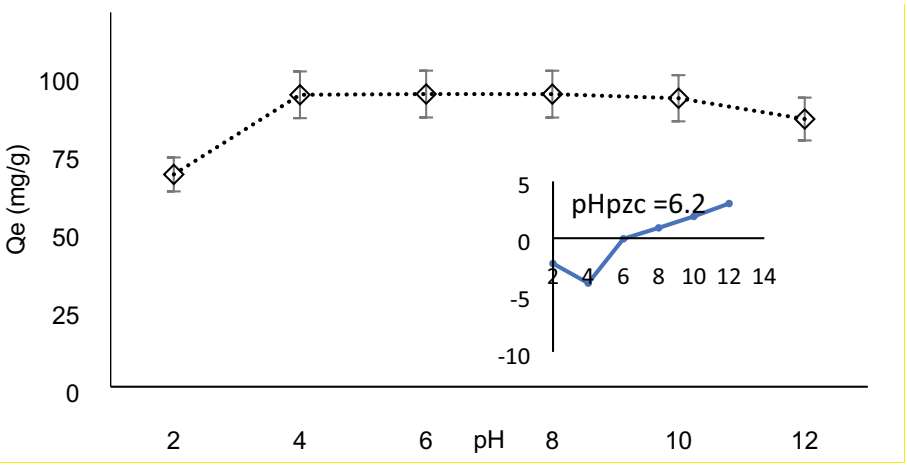

Fig. 9. Effect of pH on MG adsorption (C_0: 100 mg L^{-1}; dosage: 0.2 g; T: 30°C).

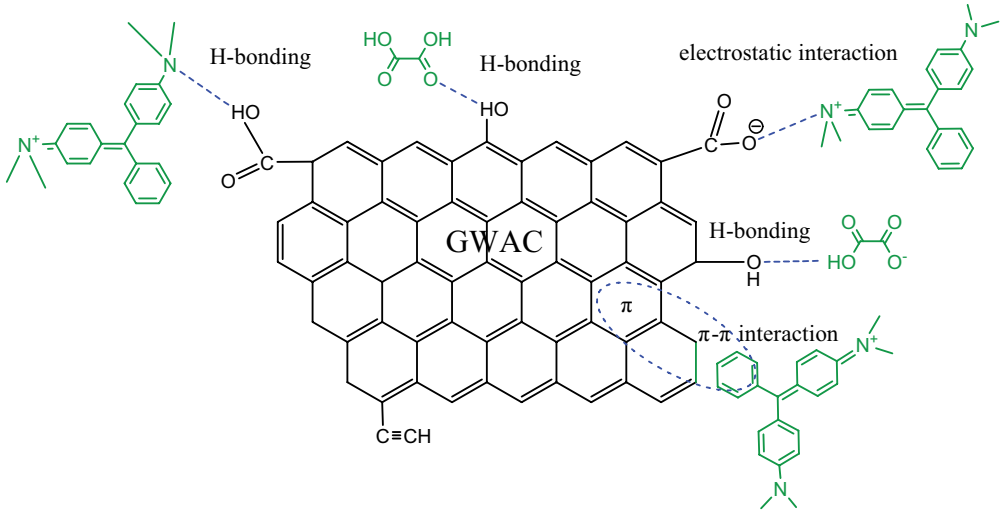

Fig. 10. Interaction mechanism of MG adsorption onto GWAC.

additional binding sites for MG sorption. As shown in Table 12, the Thomas and Yoon–Nelson models ideally fit the experimental for the flow rate and bed height of 0.5–2 ml min^{-1} and 1–3 cm, respectively. The value of q_0 predicted from these models showed good agreement with the experimental adsorption capacity, further confirming the applicability of these models to column design and analysis, indicating the adsorption process was controlled by mass transfer at the interface. A similar trend was reported by Baghdadi et al. [77], who studied MG adsorption using medical cotton waste.

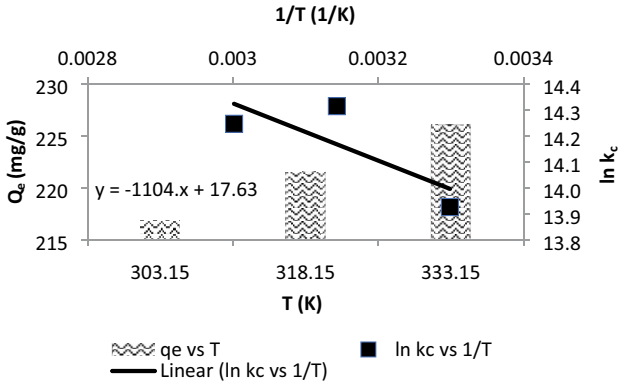

Fig. 11. Estimation of the thermodynamic parameters.

3.9. Application of GWAC for MG adsorption

3.9.1. Evaluation of adsorption efficiency using GWAC over other removal techniques

The performance of the adsorption process using GWAC was compared and summarized in Table 13. It was concluded that the adsorption process utilizing GWAC as an adsorbent has the highest removal efficiency compared to biosorption, Fenton oxidation, membrane filtration, and photodegradation. Due to its flexibility and simplicity of design, ease of operation, and high efficiency, MG adsorption using GWAC as adsorbent was proved to be superior compared to other techniques.

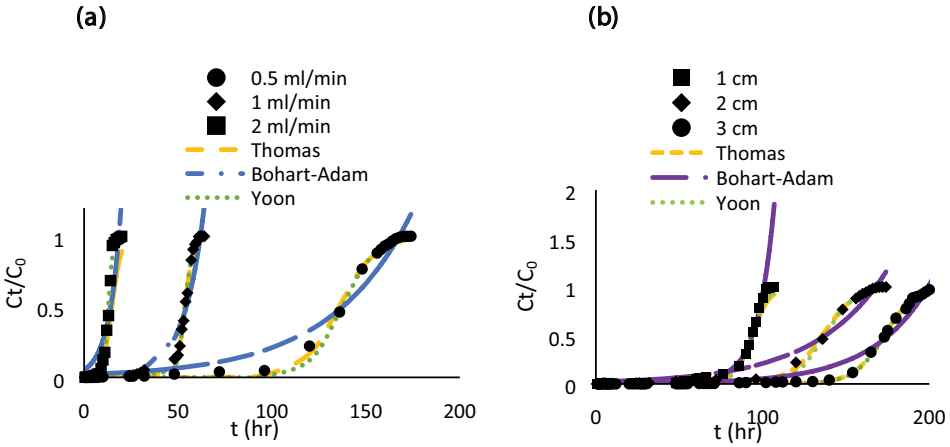

Fig. 12. Experimental and predicted breakthrough curves for MG adsorption onto GWAC at (a) different flow rates and (b) at different bed heights.

Table 12
Fixed-bed column parameters for MG adsorption by GWAC

Model	Fixed-bed length (cm)	1	2	2	2	3
	Inflow rate (ml min^{-1})	0.5	0.5	1	2	0.5
Thomas model	k_{TH} (mL mg^{-1} h^{-1})	1.899	1.019	4.522	8.383	1.086
	q_0 (mg g^{-1})	333.80	363.00	287.20	138.50	359.60
	R^2	0.9667	0.9979	0.9967	0.9965	0.9990
Yoon–Nelson model	k_{YN} (h^{-1})	0.208	0.114	0.474	0.796	0.110
	τ (h)	93.27	137.30	53.64	12.87	173.10
	q_0 (mg g^{-1})	332.71	367.44	287.10	137.77	360.12
	R^2	0.9667	0.9997	0.9963	0.9992	0.9999
Bohart–Adams model	k_{AB} × 10^{-5} (L mg^{-1} h^{-1})	99.35	23.04	92.72	158	29.42
	N_0 × 10^5 (mg L^{-1})	1.964	1.634	1.206	0.7197	1.294
	R^2	0.9831	0.9748	0.9380	0.8555	0.9760
Experimental value	q_0 (mg g^{-1})	318.99	351.12	275.04	130.71	353.23

Table 13
Comparison between the adsorption process and other MG removal methods

Process	Material used	Conditions	MG removal efficiency (%)	Disadvantage	Reference
Biosorption	Immobilized *Aspergillus niger* fungal	Dosage: 15 g L^{-1} Contact time: 72 h C_0: 15 mg L^{-1}	82.60	Longer contact time	[81]
Fenton oxidation	Iron-based nanoparticles	Dosage: 0.3 g L^{-1} C_0: 50 mg L^{-1}	93.10	Requires H_2O_2 agent, sludge generation	[82]
Membrane filtration	Eggshell	C_0: 100 mg L^{-1}	98.69	Concentrated sludge production	[83]
Photodegradation	*Ricinus communis*	Dosage: 4 g L^{-1} C_0: 40 mg L^{-1} Contact time: 90 m	85.30	Formation of by-product	[84]
Adsorption	GWAC	Dosage: 1 g L^{-1} C_0: 100 mg L^{-1} Contact time: 24 h	99.01	Requires regeneration for future used	This study

3.9.2. Comparison with other adsorbents

The values of the MG adsorption capacities are compared in Table 14. Many researchers have examined the efficiency of various low-cost adsorbents for the removal of MG dye. Comparisons of different adsorbents found in the literature were done on the basis of adsorption capacity. From the comparison, GWAC can be considered as a valuable alternative for the removal of MG from aqueous solution.

3.9.3. Economic evaluation

To study the feasibility of GWAC for commercialization, the production cost was calculated based on the cost incurred by feedstock transportation, chemicals (hydroxides and hydrochloric acid), CO_2 gas, and the electricity used when producing GWAC. Table 15 shows the estimated production cost of GWAC by KOH microwave activation. The production cost was estimated to be approximately 0.23 USD kg^{-1} of GWAC, which was significantly lower than the market price of AC (up to 5.76 USD kg^{-1} of AC) as well as other types of adsorbent, as shown in Table 16. This indicates that KOH microwave activation of GW is economically feasible for commercialization.

4. Conclusion

The optimum activation conditions for GWAC synthesis included a radiation power, time, and IR of 616 W, 1 min, and 1.06, respectively, which resulted in 89.98% yield of GWAC and 99.01% MG dye removal. In batch mode, the physical adsorption with both film and intraparticle diffusion involved satisfied the pseudo-first-order model kinetics. The equilibrium data fit well to the Fritz–Schlünder model. In continuous mode, the Thomas and Yoon–Nelson models were utilized successfully to predict MG adsorption in a fixed-bed column. The results of this study confirmed that GWAC is a promising and feasible precursor for AC production.

Acknowledgments

The authors thankfully acknowledge the support obtained from the Ministry of Higher Education (MOHE), Universiti Sains Malaysia (Research University Grant:

Table 14
Comparison of MG adsorption capacity of GWAC with other low-cost adsorbents

Adsorbent	MG adsorption capacity (mg g^{-1})	Reference
Coconut AC	91.24	[37]
Chir pine cone	250.00	[79]
Seed hull	8.40	[85]
Rice husk	24.92	[86]
Oyster mushroom	32.33	[87]
Copper pod fruit shell	62.5	[88]
Rice-bran	147.47	[89]
GWAC	226.06	This study

Table 15
Estimated production cost (USD kg^{-1}) of GWAC

Component	Estimated cost (USD kg^{-1})
Transportation cost	0.2
Chemicals (hydroxide and HCl) hydroxides = 0.01 USD, hydrochloric acid = 0.01 USD [90].	0.02
CO_2 gas, 15 USD/25 kg 1 standard refill of CO_2 gas in Malaysia = 25 kg. Total consumption = 1.5 L.	0.002
Electrical consumption (activation process) (0.616 kW × 1 min). *Charge rate of electricity in Malaysia (1 kWh) = 0.05 USD [45].	0.005
Total estimated production cost	0.227

Table 16
Comparison of estimated production cost using different feedstocks

Feedstock	Production cost (USD kg^{-1})	Reference
GWAC	0.23	This study
Banana peel	0.9	[45]
Orange peel	1.67	[90]
Artocarpus integer	0.18–0.20	[50]
Charcoal	1.72–3.84	
Wood	1.54	[91]
Pet coke	5.76	

Number 8014061 and Bridging Grant: Number: 6316195), and Universiti Malaysia Perlis (UniMAP) in the form of scholarships and facilities.

References

[1] P. González-García, Activated carbon from lignocellulosics precursors: a review of the synthesis methods, characterization techniques and applications, Renewable Sustainable Energy Rev., 82 (2018) 1393–1414.
[2] R. Tobi Ayinla, J.O. Dennis, H.M. Zaid, Y.K. Sanusi, F. Usman, L.L. Adebayo, A review of technical advances of recent palm bio-waste conversion to activated carbon for energy storage, J. Cleaner Prod., 229 (2019) 1427–1442.
[3] S. Hajati, M. Ghaedi, S. Yaghoubi, Local, cheep and nontoxic activated carbon as efficient adsorbent for the simultaneous removal of cadmium ions and malachite green: optimization by surface response methodology, J. Ind. Eng. Chem., 21 (2015) 760–767.
[4] N. Saman, A. Abdul Aziz, K. Johari, S.-T. Song, H. Mat, Adsorptive efficacy analysis of lignocellulosic waste carbonaceous adsorbents toward different, Process Saf. Environ. Prot., 96 (2015) 33–42.
[5] M. Ghaedi, H. Mazaheri, S. Khodadoust, S. Hajati, M.K. Purkait, Application of central composite design for simultaneous removal of methylene blue and Pb^{2+} ions by walnut wood activated carbon, Spectrochim. Acta, Part A, 135 (2015) 479–490.
[6] S. Sangon, A.J. Hunt, T.M. Attard, P. Mengchang, Y. Ngernyen, N. Supanchaiyamat, Valorisation of waste rice straw for the production of highly effective carbon based adsorbents for dyes removal, J. Cleaner Prod., 172 (2018) 1128–1139.
[7] A.P. de Oliveira, A.N. Módenes, M.E. Bragião, C.L. Hinterholz, D.E.G. Trigueros, I.G. de O. Bezerra, Use of grape pomace as a biosorbent for the removal of the Brown KROM KGT dye, Bioresour. Technol. Rep., 2 (2018) 92–99.
[8] S.K. Low, M.C. Tan, Dye adsorption characteristic of ultrasound pre-treated pomelo peel, J. Environ. Chem. Eng., 6 (2018) 3502–3509.
[9] H.T. Van, L.H. Nguyen, V.D. Nguyen, X.H. Nguyen, T.H. Nguyen, T.V. Nguyen, S. Vigneswaran, J. Rinklebe, H.N. Tran, Characteristics and mechanisms of cadmium adsorption onto biogenic aragonite shells-derived biosorbent: batch and column studies, J. Environ. Manage., 241 (2019) 535–548.
[10] A. Khasri, O.S. Bello, M.A. Ahmad, Mesoporous activated carbon from *Pentace* species sawdust via microwave-induced KOH activation: optimization and methylene blue adsorption, Res. Chem. Intermed., 44 (2018) 5737–5757.
[11] N.A. Rashidi, S. Yusup, A review on recent technological advancement in the activated carbon production from oil palm wastes, Chem. Eng. J., 314 (2017) 277–290.
[12] A. Pandiarajan, R. Kamaraj, S. Vasudevan, S. Vasudevan, OPAC (orange peel activated carbon) derived from waste orange peel for the adsorption of chlorophenoxyacetic acid herbicides from water: adsorption isotherm, kinetic modelling and thermodynamic studies, Bioresour. Technol., 261 (2018) 329–341.
[13] K. Sartova, E. Omurzak, G. Kambarova, I. Dzhumaev, B. Borkoev, Activated carbon obtained from the cotton processing wastes, Diamond Relat. Mater., 91 (2019) 90–97.
[14] D.Q. Tian, Z.H. Xu, D.F. Zhang, W.F. Chen, J.L. Cai, H.X. Deng, Z.H. Sun, Y.W. Zhou, Micro–mesoporous carbon from cotton waste activated by $FeCl_3/ZnCl_2$: preparation, optimization, characterization and adsorption of methylene blue and eriochrome black T, J. Solid State Chem., 269 (2019) 580–587.
[15] IMARC Group, Biomass Gasification Market: Global Industry Trends, Share, Size, Growth, Opportunity and Forecast 2018–2023, IMARC Group, United States, 2017.
[16] V. Benedetti, F. Patuzzi, M. Baratieri, Characterization of char from biomass gasification and its similarities with activated carbon in adsorption applications, Appl. Energy, 227 (2018) 92–99.
[17] M. Galhetas, A.S. Mestre, M.L. Pinto, I. Gulyurtlu, H. Lopes, A.P. Carvalho, Chars from gasification of coal and pine activated with K_2CO_3: Acetaminophen and caffeine adsorption from aqueous solutions, J. Colloid Interface Sci., 433 (2014) 2014.
[18] T. Maneerung, J. Liew, Y.J. Dai, S. Kawi, C. Chong, C.-H. Wang, Activated carbon derived from carbon residue from biomass gasification and its application for dye adsorption: kinetics, isotherms and thermodynamic studies, Bioresour. Technol., 200 (2016) 350–359.
[19] S.J. Culp, F.A. Beland, Malachite green: a toxicological review, J. Am. Coll. Toxicol., 15 (1996) 219–238.
[20] P.P. Kwan, S. Banerjee, M. Shariff, N.A.S. Ishak, F.M. Yusoff, Quantitative analysis of malachite green and leucomalachite green residues in fish purchased from the markets in Malaysia, Food Control, 92 (2018) 101–106.
[21] S.N. Jain, P.R. Gogate, Efficient removal of Acid Green 25 dye from wastewater using activated *Prunus Dulcis* as biosorbent: batch and column studies, J. Environ. Manage., 210 (2018) 226–238.
[22] M. de la Luz-Asunción, E.E. Pérez-Ramírez, A.L. Martínez-Hernández, V.M. Castano, V. Sánchez-Mendieta, C. Velasco-Santos, Non-linear modeling of kinetic and equilibrium data for the adsorption of hexavalent chromium by carbon

nanomaterials: dimension and functionalization, Chin. J. Chem. Eng., 27 (2019) 912–919.
[23] M.-H. To, P. Hadi, C.-W. Hui, C.S.K. Lin, G. McKay, Mechanistic study of atenolol, acebutolol and carbamazepine adsorption on waste biomass derived activated carbon, J. Mol. Liq., 241 (2017) 386–398.
[24] N. Ayawei, A.N. Ebelegi, D. Wankasi, Modelling and interpretation of adsorption isotherms, J. Chem., 2017 (2017) 1–11.
[25] M.K. Dahri, M.R.R. Kooh, L.B.L. Lim, Water remediation using low cost adsorbent walnut shell for removal of malachite green: equilibrium, kinetics, thermodynamic and regeneration studies, J. Environ. Chem. Eng., 2 (2014) 1434–1444.
[26] K.C. Nebaghe, Y. El Boundati, K. Ziat, A. Naji, L. Rghioui, M. Saidi, Comparison of linear and non-linear method for determination of optimum equilibrium isotherm for adsorption of copper(II) onto treated Martil sand, Fluid Phase Equilib., 430 (2016) 188–194.
[27] L.C. Zheng, Y.B. Yang, P.P. Meng, D. Peng, Absorption of cadmium (II) via sulfur-chelating based cellulose: characterization, isotherm models and their error analysis, Carbohydr. Polym., 209 (2019) 38–50.
[28] F. Gritti, G. Guiochon, New thermodynamically consistent competitive adsorption isotherm in RPLC, J. Colloid Interface Sci., 264 (2003) 43–59.
[29] M. Wakkel, B. Khiari, F. Zagrouba, Textile wastewater treatment by agro-industrial waste: equilibrium modelling, thermodynamics and mass transfer mechanisms of cationic dyes adsorption onto low-cost lignocellulosic adsorbent, J. Taiwan Inst. Chem. Eng., 96 (2019) 439–452.
[30] A.K. Nayak, A. Pal, Development and validation of an adsorption kinetic model at solid-liquid interface using normalized Gudermannian function, J. Mol. Liq., 276 (2019) 67–77.
[31] J.O. Babalola, B.A. Koiki, Y. Eniayewu, A. Salimonu, J.O. Olowoyo, V.O. Oninla, H.A. Alabi, A.E. Ofomaja, M.O. Omorogie, Adsorption efficacy of *Cedrela odorata* seed waste for dyes: non linear fractal kinetics and non linear equilibrium studies, J. Environ. Chem. Eng., 4 (2016) 3527–3536.
[32] S. Batra, D. Datta, N.S. Beesabathuni, N. Kanjolia, S. Saha, Adsorption of bisphenol-A from aqueous solution using amberlite XAD-7 impregnated with aliquat 336: batch, column, and design studies, Process Saf. Environ. Prot., 122 (2019) 232–246.
[33] A. Syafiuddin, S. Salmiati, J. Jonbi, M.A. Fulazzaky, Application of the kinetic and isotherm models for better understanding of the behaviors of silver nanoparticles adsorption onto different adsorbents, J. Environ. Manage., 218 (2018) 59–70.
[34] M.K. Dahri, M.R.R. Kooh, L.B.L. Lim, Application of *Casuarina equisetifolia* needle for the removal of methylene blue and malachite green dyes from aqueous solution, Alexandria Eng. J., 54 (2015) 1253–1263.
[35] P. Saha, S. Chowdhury, Insight Into Adsorption Thermodynamics, in: Thermodynamics, InTech Europe, 2011, pp. 349–364.
[36] A. Ebadi, J.S. Soltan Mohammadzadeh, A. Khudiev, What is the correct form of BET isotherm for modeling liquid phase adsorption?, Adsorption, 15 (2009) 65–73.
[37] W.Y. Qu, T. Yuan, G.J. Yin, S. Xu, Q. Zhang, H.J. Su, Effect of properties of activated carbon on malachite green adsorption, Fuel, 249 (2019) 45–53.
[38] E.C. Lima, A. Hosseini-Bandegharaei, J.C. Moreno-Piraján, I. Anastopoulos, A critical review of the estimation of the thermodynamic parameters on adsorption equilibria. Wrong use of equilibrium constant in the Van't Hoof equation for calculation of thermodynamic parameters of adsorption, J. Mol. Liq., 273 (2019) 425–434.
[39] Y. Liu, Is the free energy change of adsorption correctly calculated?, J. Chem. Eng. Data, 54 (2009) 1981–1985.
[40] L. Lonappan, T. Rouissi, Y. Liu, S.K. Brar, R.Y. Surampalli, Removal of diclofenac using microbiochar fixed-bed column bioreactor, J. Environ. Chem. Eng., 7 (2019) 102894.
[41] J. Jang, D.S. Lee, Effective phosphorus removal using chitosan/Ca-organically modified montmorillonite beads in batch and fixed-bed column studies, J. Hazard. Mater., 375 (2019) 9–18.
[42] M.A. Ahmad, R. Alrozi, Optimization of preparation conditions for mangosteen peel-based activated carbons for the removal of Remazol Brilliant Blue R using response surface methodology, Chem. Eng. J., 165 (2010) 883–890.
[43] I.A.W. Tan, A.L. Ahmad, B.H. Hameed, Optimization of preparation conditions for activated carbons from coconut husk using response surface methodology, Chem. Eng. J., 137 (2008) 462–470.
[44] T. Yang, A.C. Lua, Characteristics of activated carbons prepared from pistachio-nut shells by physical activation, J. Colloid Interface Sci., 267 (2003) 408–417.
[45] R.K. Liew, E. Azwar, P.N.Y. Yek, X.Y. Lim, C.K. Cheng, J.-H. Ng, A. Jusoh, W.H. Lam, M.D. Ibrahim, N.L. Ma, S.S. Lam, Microwave pyrolysis with KOH/NaOH mixture activation: a new approach to produce micro-mesoporous activated carbon for textile dye adsorption, Bioresour. Technol., 266 (2018) 1–10.
[46] S.S. Lam, R.K. Liew, Y.M. Wong, E. Azwar, A. Jusoh, R. Wahi, Activated carbon for catalyst support from microwave pyrolysis of orange peel, Waste Biomass Valorization, 8 (2017) 2109–2119.
[47] M.A. Ahmad, N.S. Afandi, O.S. Bello, Optimization of process variables by response surface methodology for malachite green dye removal using lime peel activated carbon, Appl. Water Sci., 7 (2015) 717–727.
[48] M. Makeswari, T. Santhi, Removal of malachite green dye from aqueous solutions onto microwave assisted zinc chloride chemical activated epicarp of *Ricinus communis*, J. Water Resour. Prot., 5 (2013) 222–238.
[49] A.A.A. Zuki, M. Awang, A.A. Mahmud, M.H. Zain, J.J. Jaafar, Adsorption of malachite green dye on microwave and chemically treated *Casuarina equisetifolia* seeds as an eco-friendly adsorbent, Adv. Environ. Biol., 9 (2015) 216–223.
[50] S.S. Lam, R.K. Liew, Y.M. Wong, P.N.Y. Yek, N.L. Ma, C.L. Lee, H.A. Chase, Microwave-assisted pyrolysis with chemical activation, an innovative method to convert orange peel into activated carbon with improved properties as dye adsorbent, J. Cleaner Prod., 162 (2017) 1376–1387.
[51] K.S.W. Sing, D.H. Everett, R.A.W. Haul, L. Moscou, R.A. Pierotti, J. Rouquérol, T. Siemieniewska, Reporting physisorption data for gas/solid systems with special reference to the determination of surface area and porosity, Pure Appl. Chem., 57 (1985) 603–619.
[52] A.E. Ogungbenro, D.V. Quang, K.A. Al-Ali, L.F. Vega, M.R.M. Abu-Zahra, Physical synthesis and characterization of activated carbon from date seeds for CO_2 capture, J. Environ. Chem. Eng., 6 (2018) 4245–4252.
[53] J.-X. Yang, G.-B. Hong, Adsorption behavior of modified *Glossogyne tenuifolia* leaves as a potential biosorbent for the removal of dyes, J. Mol. Liq., 252 (2018) 289–295.
[54] K.Y. Foo, B.H. Hameed, Porous structure and adsorptive properties of pineapple peel based activated carbons prepared via microwave assisted KOH and K_2CO_3 activation, Microporous Mesoporous Mater., 148 (2012) 191–195.
[55] K.Y. Foo, B.H. Hameed, Preparation and characterization of activated carbon from sunflower seed oil residue via microwave assisted K_2CO_3 activation, Bioresour. Technol., 102 (2011) 9794–9799.
[56] J. Pallarés, A. González-cencerrado, I. Arauzo, Production and characterization of activated carbon from barley straw by physical activation with carbon dioxide and steam, Biomass Bioenergy, 115 (2018) 64–73.
[57] X. Song, R. Xu, K. Wang, High capacity adsorption of malachite green in a mesoporous tyre-derived activated carbon, Asia-Pac. J. Chem. Eng., 8 (2013) 172–177.
[58] S. Pandia, A.T. Hutagalung, A.D. Siahaan, Utilization of cocoa peel as biosorbent for oil and color removal in palm oil mill effluent (POME), IOP Conf. Ser.: Mater. Sci. Eng., 300 (2018), doi: 10.1088/1757-899X/300/1/012066.
[59] S. Maulina, S. Iriansyah, Characteristics of activated carbon resulted from pyrolysis of the oil palm fronds powder, IOP Conf. Ser.: Mater. Sci. Eng., 309 (2018), doi: 10.1088/1757-899X/309/1/012072.
[60] J. Bedia, M. Peñas-Garzón, A. Gómez-Avilés, J.J. Rodríguez, C. Belver, A review on the synthesis and characterization of biomass-derived carbons for adsorption of emerging

contaminants from water, J. Carbon Res., 4 (2018) 63, https://doi.org/10.3390/c4040063.
[61] F. Hanum, O. Bani, L.I. Wirani, Characterization of activated carbon from rice husk by HCl activation and its application for lead (Pb) removal in car battery wastewater, IOP Conf. Ser.: Mater. Sci. Eng., 180 (2017), doi: 10.1088/1757-899X/180/1/012151.
[62] J. Yang, K.Q. Qiu, Development of high surface area mesoporous activated carbons from herb residues, Chem. Eng. J., 167 (2011) 148–154.
[63] N. Khadhri, M. El Khames Saad, M. Ben Mosbah, Y. Moussaoui, Batch and continuous column adsorption of indigo carmine onto activated carbon derived from date palm petiole, J. Environ. Chem. Eng., 7 (2019) 102775.
[64] T. Haeldermans, J. Claesen, J. Maggen, R. Carleer, J. Yperman, P. Adriaensens, P. Samyn, D. Vandamme, A. Cuypers, K. Vanreppelen, S. Schreurs, Microwave assisted and conventional pyrolysis of MDF – characterization of the produced biochars, J. Anal. Appl. Pyrolysis, 138 (2019) 218–230.
[65] S. Rattanapan, J. Srikram, P. Kongsune, Adsorption of methyl orange on coffee grounds activated carbon, Energy Procedia, 138 (2017) 949–954.
[66] C.G. Joseph, J. Janaun, M. Massuanna, Removal of malachite green from aqueous solution by waste tyre derived activated carbon, Malaysian J. Chem., 17 (2015) 16–28.
[67] Y. Gokce, Z. Aktas, Nitric acid modification of activated carbon produced from waste tea and adsorption of methylene blue and phenol, Appl. Surf. Sci., 313 (2014) 352–359.
[68] M. Uchimiya, A. Orlov, G. Ramakrishnan, K. Sistani, In situ and ex situ spectroscopic monitoring of biochar's surface functional groups, J. Anal. Appl. Pyrolysis, 102 (2013) 53–59.
[69] K.F. Fu, Q.Y. Yue, B.Y. Gao, Y. Wang, Q. Li, Activated carbon from tomato stem by chemical activation with $FeCl_2$, Colloids Surf., A, 529 (2017) 842–849.
[70] O.A. Ioannidou, A.A. Zabaniotou, G.G. Stavropoulos, A. Islam, T.A. Albanis, Preparation of activated carbons from agricultural residues for pesticide adsorption, Chemosphere, 80 (2010) 1328–1336.
[71] T.-H. Liou, S.-J. Wu, Characteristics of microporous/mesoporous carbons prepared from rice husk under base- and acid-treated conditions, J. Hazard. Mater., 171 (2009) 693–703.
[72] L.M. Mosley, P. Willson, B. Hamilton, G. Butler, R. Seaman, The capacity of biochar made from common reeds to neutralise pH and remove dissolved metals in acid drainage, Environ. Sci. Pollut. Res., 22 (2015) 15113–15122.
[73] H.Y. Zhang, Z.W. Wang, R.N. Li, J.L. Guo, Y. Li, J.M. Zhu, X.Y. Xie, TiO_2 supported on reed straw biochar as an adsorptive and photocatalytic composite for the efficient degradation of sulfamethoxazole in aqueous matrices, Chemosphere, 185 (2017) 351–360.
[74] D. Xin-Hui, C. Srinivasakannan, P. Jin-Hui, Z. Li-Bo, Z. Zheng-Yong, Preparation of activated carbon from Jatropha hull with microwave heating: optimization using response surface methodology, Fuel Process. Technol., 92 (2011) 394–400.
[75] R. Soltani, A. Marjani, S. Shirazian, Facile one-pot synthesis of thiol-functionalized mesoporous silica submicrospheres for Tl(I) adsorption: isotherm, kinetic and thermodynamic studies, J. Hazard. Mater., 371 (2019) 146–155.
[76] O.S. Bello, Adsorptive removal of malachite green with activated carbon prepared from oil palm fruit fibre by KOH activation and CO_2 gasification, South Africa J. Chem., 66 (2013) 32–41.
[77] M. Baghdadi, B. Alipour Soltani, M. Nourani, Malachite green removal from aqueous solutions using fibrous cellulose sulfate prepared from medical cotton waste: comprehensive batch and column studies, J. Ind. Eng. Chem., 55 (2017) 128–139.
[78] T.P. Krishna Murthy, B.S. Gowrishankar, M.N. Chandra Prabha, M. Kruthi, R. Hari Krishna, Studies on batch adsorptive removal of malachite green from synthetic wastewater using acid treated coffee husk: equilibrium, kinetics and thermodynamic studies, Microchem. J., 146 (2019) 192–201.
[79] G. Sharma, S. Sharma, A. Kumar, M. Naushad, B. Du, T. Ahamad, A.A. Ghfar, A.A. Alqadami, F.J. Stadler, Honeycomb structured activated carbon synthesized from *Pinus roxburghii* cone as effective bioadsorbent for toxic malachite green dye, J. Water Process Eng., 32 (2019) 100931.
[80] F. Bouaziz, M. Koubaa, F. Kallel, R.E. Ghorbel, S.E. Chaabouni, Adsorptive removal of malachite green from aqueous solutions by almond gum: kinetic study and equilibrium isotherms, Int. J. Biol. Macromol., 105 (2017) 56–65.
[81] V. Katheresan, J. Kansedo, S.Y. Lau, Efficiency of various recent wastewater dye removal methods: a review, J. Environ. Chem. Eng., 6 (2018) 4676–4697.
[82] Y. Wu, S.L. Zeng, F.F. Wang, M. Megharaj, R. Naidu, Z.L. Chen, Heterogeneous Fenton-like oxidation of malachite green by iron-based nanoparticles synthesized by tea extract as a catalyst, Sep. Purif. Technol., 154 (2015) 161–167.
[83] H.M. Chen, J. Liu, X.Z. Cheng, Y. Peng, Adsorption for the removal of malachite green by using eggshell membrane in environment water samples, Adv. Mater. Res., 573–574 (2012) 63–67.
[84] V. Nirmaladevi, M. Makeswari, T. Santhi, malachite green dye degradation using $ZnCl_2$ activated *Ricinus communis* stem by sunlight irradiation, Rasayan J. Chem., 11 (2018) 219–227.
[85] M. Mohammad, S. Maitra, B.K. Dutta, Comparison of activated carbon and physic seed hull for the removal of malachite green dye from aqueous solution, Water Air Soil Pollut., 229 (2018) 1–14.
[86] S. Chowdhury, R. Mishra, P. Saha, P. Kushwaha, Adsorption thermodynamics, kinetics and isosteric heat of adsorption of malachite green onto chemically modified rice husk, Desalination, 265 (2011) 159–168.
[87] Z.S. Chen, H.B. Deng, C. Chen, Y. Yang, H. Xu, Biosorption of malachite green from aqueous solutions by *Pleurotus ostreatus* using Taguchi method, J. Environ. Health Sci. Eng., 12 (2014) 1–10.
[88] S. Rangabhashiyam, P. Balasubramanian, Performance of novel biosorbents prepared using native and NaOH treated *Peltophorum pterocarpum* fruit shells for the removal of malachite green, Bioresour. Technol. Rep., 3 (2018) 75–81.
[89] H.N. Bhatti, A. Jabeen, M. Iqbal, S. Noreen, Z. Naseem, Adsorptive behavior of rice bran-based composites for malachite green dye: isotherm, kinetic and thermodynamic studies, J. Mol. Liq., 237 (2017) 322–333.
[90] G. Selvaraju, N.K.A. Bakar, Production of a new industrially viable green-activated carbon from *Artocarpus integer* fruit processing waste and evaluation of its chemical, morphological and adsorption properties, J. Cleaner Prod., 141 (2017) 989–999.
[91] G.G. Stavropoulos, A.A. Zabaniotou, Minimizing activated carbons production cost, Fuel Process. Technol., 90 (2009) 952–957.